ACS OMEGA

Open Access

http://pubs.acs.org/journal/acsodf

Article

PVA-Stabilized and Coassembled Nano/Microparticles with High Payload of Dual Phytochemicals for Enhanced Antibacterial and Targeting Effect

Hua Yang,[‖] Yuerui Yang,[‖] Jiao Wang, Zhi Dong, Jiali Wang, Yuhua Ma, Peng Zhang,* and Wenping Wang*

Cite This: *ACS Omega* 2024, 9, 41990−42001

Read Online

ACCESS | Metrics & More | Article Recommendations | Supporting Information

ABSTRACT: The codelivery of multiple bioactive phytochemicals via nano/microparticles (NPs/MPs) represents a promising strategy for enhancing therapeutic efficacy. This study presents the development of novel poly(vinyl alcohol) (PVA)-stabilized hybrid particles designed for codelivery of palmatine hydrochloride (PAL) and glycyrrhizic acid (GL). Employing a straightforward coassembly method, we synthesized dual-drug particles achieving a high payload capacity of over 70%. The particles were characterized as uniform in size, within the nano/micron range, and exhibited a ζ-potential of −5.0 mV. The incorporation of PVA not only stabilized the particles but also refined the aggregation process, resulting in more uniform and finer particles approximately 1 μm in size. Spectral analysis and molecular dynamics simulations verified the presence of $\pi-\pi$ stacking and hydrogen bonding between PAL and GL within the particles. In vitro antibacterial assays indicated that the hybrid particles had a lower minimum inhibitory concentration against *Escherichia coli* and Multidrug-Resistant *Staphylococcus aureus* than those of the pure drugs. *In vivo* biodistribution study in rats revealed that the PVA-stabilized particles revealed enhanced targeting to the liver, lung, and heart, demonstrating improved tissue selectivity compared with the solution group. In summary, the PVA-stabilized hybrid NPs/MPs represent an innovative and efficient platform for codelivery of multidrugs. These findings highlight the promise of coassembled particles for high loading, enhanced bioactivity, and targeted delivery, making them a strong candidate for future clinical applications.

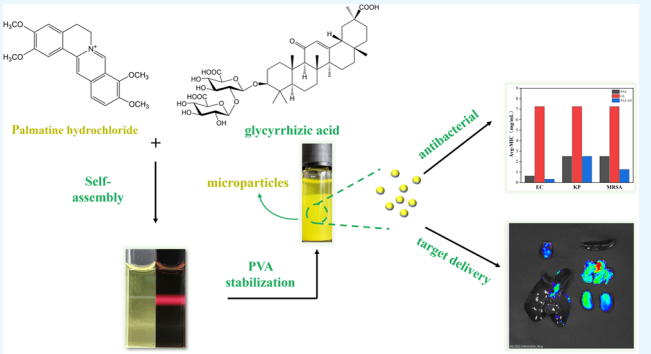

INTRODUCTION

Micro- and nanotechnologies have been extensively explored for their potential as innovative platforms in drug delivery, particularly for bioactive phytochemicals.[1] Nano/microparticles (NPs/MPs), typically sized between 1 and 1000 μm, are acknowledged for their ability to enhance the physicochemical properties and therapeutic efficacy of various drugs.[2,3] By manipulating factors such as particle size, shape, or surface charge, NPs/MPs can be engineered to deliver active substances to specific *in vivo* sites, making them a powerful tool in targeted drug delivery.[4]

Selecting appropriate carrier materials and fabrication methods is crucial for ensuring effective drug incorporation and imparting specific characteristics to the final product. Traditionally, polymers have been used to form a matrix for drug encapsulation,[5] resulting in particles with relatively low drug loading (DL) capacities, often below 20%.[6] The production of these particles frequently necessitates the use of toxic organic solvents, costly equipment, or extreme conditions, which can affect the safety, stability, and cost-effectiveness of the MP products.[7] Therefore, there is a clear need for innovative strategies that can increase loading capacity and simplify the fabrication process.

The use of combination therapy with multiple drugs is a strategic approach to achieving synergistic effects or reducing side effects. The potential for enhancing the pharmaceutical performance through interactions among different drugs is significant. Recently, pure drug NPs have attracted considerable interest due to their carrier-free formulation and straightforward nanoprecipitation process.[8−11] Multidrug combinations can form uniform nanoparticles through supramolecular assembly, leading to excellent therapeutic outcomes in anticancer and antibacterial applications.[12−14] However, the

Received: July 29, 2024
Revised: September 9, 2024
Accepted: September 17, 2024
Published: September 26, 2024

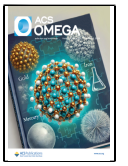

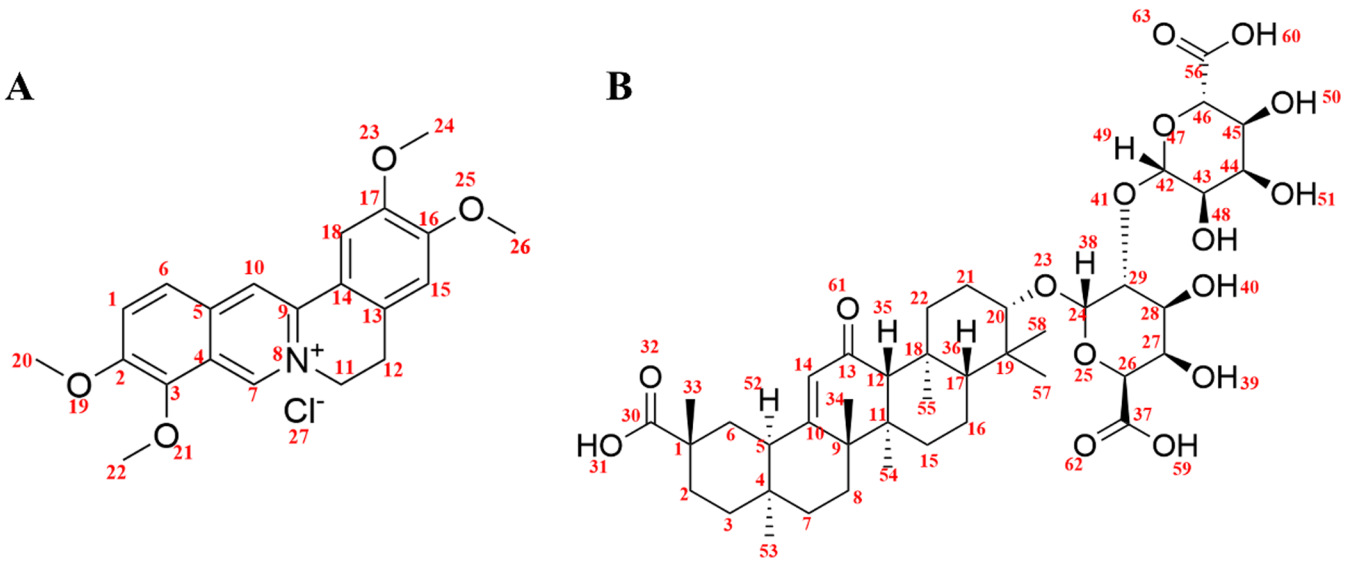

Figure 1. Chemical structure of (A) palmatine hydrochloride and (B) glycyrrhizic acid.

application of coassembly strategies for designing drug-loaded particles/MPs has been minimally explored.

Palmatine (PAL), an isoquinoline alkaloid (see Figure 1A) found in various botanical species, has been used in traditional Asian medicine for centuries.[15] The Chinese Pharmacopoeia recognizes PAL as an antibacterial and anti-inflammatory agent for the treatment of various infectious diseases.[16] Another natural product, glycyrrhizic acid (GL), is a pentacyclic saponin derived from the renowned medicinal herb licorice.[17] GL exhibits a spectrum of biological activities, including antibacterial, anti-inflammatory, anticancer, hepatoprotective, and nephroprotective effects, and is also beneficial in the treatment of pulmonary arterial hypertension.[17] As a natural amphiphilic compound consisting of a glucuronic acid and glycyrrhetic acid, GL (see Figure 1B) can spontaneously form micelles or gels through supramolecular self-assembly in aqueous media.[18] This property has led to its widespread application as a multifunctional carrier material for the solubilization and nanoencapsulation of poorly soluble drugs.[19] Additionally, GL has been identified as a specific ligand for targeting nanosystems, thereby enhancing the treatment of liver cancer.[20] Considering that PAL is a quaternary compound and GL contains multiple reactive phenolic hydroxyl groups, both characterized by complex aromatic ring structures,[21] we propose that PAL and GL may coassemble to create a new configuration, potentially enhancing their pharmaceutical and therapeutic properties.

This study aimed to develop a novel PAL-GL hybrid NPs/MPs formulation to enhance the payload capacity and streamline the fabrication process. The interactions between the two drugs were assessed by using both experimental and theoretical methods. Poly(vinyl alcohol) (PVA) was employed as a polymeric stabilizer to regulate particle size. The resulting NPs/MPs were evaluated for their physicochemical properties, antibacterial activity, and in vivo tissue distribution performance, offering a comprehensive assessment of their potential as a targeted drug delivery system.

EXPERIMENTAL METHODS

Materials. Palmatine hydrochloride and glycyrrhizic acid (purity >98%) were supplied by Jingzhu Biotech Co., Ltd. (Nanjing, China). Poly(vinyl alcohol) (PVA, 1788) was purchased from Aladdin Biotech Co., Ltd. (Shanghai, China). Methanol and acetonitrile were of high-pressure liquid chromatography (HPLC) grade, and other chemicals were of analytical grade and used as received. All solutions were prepared using purified or ultrapurified water provided by Arium Comfort II system (Sartorius, Germany).

Bacterial strains, including *Escherichia coli* (EC) ATCC 25922, *Staphylococcus aureus* (SA) ATCC 6583, methicillin-resistant *Staphylococcus aureus* (MRSA) ATCC 43300, *Klebsiella pneumoniae* (KP) ATCC 13883, and *Pseudomonas aeruginosa* (PA) ATCC 9027, were supplied by the Guangdong Microbial Culture Collection Center (GDMCC). Luria–Bertani (LB) solid medium, used for culturing the bacterial strains, was purchased from Huankai Microbial Science and Technology (Guangdong, China). Ciprofloxacin hydrochloride, employed as a positive control antibiotic, was sourced from Jingxin Pharmaceutical Co., Ltd (Zhejiang, China). 2,3,5-Triphenyltetrazolium chloride (TTC) was provided by Rhawn (Shanghai, China).

Methods. *Preparation of Hybrid Microparticles.* The precipitation behavior of mixed aqueous systems was observed to determine the optimal drug solution concentration for MPs formation. Bulk powders of PAL or GL were dissolved in water and heated to 80 °C. The resulting solutions were then mixed in various molar ratios in a 96-well plate. The optical density (OD) of the mixtures at 600 nm was measured at 5 min and 24 h postmixing using a Spark 10 M multimode microplate reader (Tecan, Shanghai). The mixtures were also visually inspected for any signs of turbidity or sedimentation and further observed under *a* CKX53 microscope (Olympus, China).

The hybrid NPs/MPs of PAL and GL were prepared by using a simple solution-mixing method. Briefly, PAL (24 mM) or GL (12 mM) was dissolved in purified water to form the drug solution. PVA (4 mg/mL) was then dispersed into the PAL solution. Both solutions were heated separately to 80 °C before being mixed in a volumetric ratio of 1:1. The mixture was then cooled to room temperature and stored in a refrigerator overnight. The resulting suspension was centrifuged at 10 000 rpm for 5 min to collect the particles, which were then freeze-dried for 48 h by a Scientz-10N vacuum

https://doi.org/10.1021/acsomega.4c06925
ACS Omega 2024, 9, 41990−42001

freeze-dryer (Ningbo Scientz Biotechnology Co., Ltd., Ningbo, China) and sieved through a 100-mesh screen.

The samples without PVA or coloaded with Rhodamine B were prepared following the same procedure for comparative analysis. All of the resultant powders were stored at room temperature in a desiccator containing anhydrous silica gel until use.

Particle Morphology. The morphological changes in the drug solutions before and after mixing were visually assessed. All samples were further examined using scanning electron microscopy (SEM, Phenom Pro, Thermo Fisher Scientific, Waltham, MA). Freshly prepared suspensions of the hybrid NPs/MPs were dropped onto a holder and allowed to dry at room temperature before observation. Powders of the pure drugs were directly spread on a holder before metallization and then observed at an acceleration voltage of 10 kV in the backscattered electron mode.

Particle Size Distribution and ζ-Potential Analysis. The obtained samples were analyzed for their particle size distribution and ζ-potential using dynamic light scattering (DLS) equipment (NanoBrook 90 plus, Brookhaven Instrument, NY). Prior to testing, the freshly prepared solutions and suspensions were diluted to a concentration of 0.01 mg/mL with water and the dry powders were redispersed in water and sonicated for 3 min. All samples were tested at a scattering angle of 90° and a wavelength of 500 nm.

Thermal Analysis. The thermal properties of the samples were evaluated by an X'Pert PRO differential scanning calorimeter (DSC, Spectris, Holland). Approximately 5 mg of powdered sample was sealed in aluminum pans and heated from 25 to 400 °C at a rate of 10 °C/min under a nitrogen atmosphere. The DSC and DTG curves of various samples were analyzed and compared.

Powder X-ray Diffraction (PXRD). The crystalline state of the samples was accessed using a D8 Advance X-ray diffractometer (Bruker, Germany) with Cu−Kα radiation. Data were collected over the 2θ range of 5−85° at a scanning rate of 8°/min with a step size of 0.02°. Tube voltage and current were set at 40 kV and 30 mA, respectively. JADE 6.5 software was used to analyze the resulting PXRD patterns.

Fourier Transform Infrared (FTIR) Spectroscopy. Powder samples were mixed with KBr pellets in an agate mortar, pressed into thin disks, and characterized by a Great20 ATR-FTIR spectrometer (CKRG, China) under the following conditions: scanning range of 4000−400 cm^{-1}; wavenumber resolution of 2 cm^{-1}; operating mode in transmission percentage; and 64 cumulative scans at room temperature.

Ultraviolet−Visible (UV−Vis) Spectroscopy. The solutions of various samples were prepared by dissolving bulk drugs or powdered MPs in methanol, respectively. The absorption spectra of each solution were recorded using a T6 UV−vis spectrophotometer (Pgeneral Lt., Beijing, China) in a quartz cell with a 10 mm path length. All solutions were scanned over a range of 200−600 nm with a fixed slit width of 1 nm.

Nuclear Magnetic Resonance Hydrogen Spectrometry (^{1}H NMR) Analysis. Powders of pure drugs (10 mg) or their MPs (15 mg) were fully dissolved in 0.5 mL of deuterium dimethyl sulfoxide (DMSO-d_6). The resulting solutions were then scanned 32 times by a Bruker Advance 400 MHz NMR apparatus (Bruker, Germany) with tetramethylsilane as an internal standard.

Drug Content. Powder samples (5 mg) were accurately weighed and completely dissolved in 10 mL of methanol. Drug concentration in the resulting solution was determined by a high-pressure liquid chromatography (HPLC) system equipped with a C18 column (250 × 4.6 mm × 5 μm, Agilent). The chromatographic separation was achieved using a mobile phase composed of acetonitrile (A) and 0.05% phosphoric acid (B) by a gradient elution at 1.0 mL/min. The detection wavelengths were set at 254 nm for PAL and 345 nm for GL, respectively. The drug loading (DL) of MPs was calculated according to eq 1

$$\mathrm{DL}\ (\%) = (\text{mass of drug in particles}/\text{mass of total particles}) \times 100\% \quad (1)$$

Molecular Dynamic (MD) Simulation. Molecular dynamic (MD) simulations were conducted to investigate the intermolecular interactions between PAL and GL and to elucidate the coassembly behavior of drug molecules using Gromacs 2202.6 program.[22]

The potential interactions of various drug−drug dimers were analyzed using Molclus 1.9[23] software, with visualizations rendered by Multiwfn[24] and VMD.[25] Typically, a set of 100 conformations for each dimer were generated using Genmer with an rmax value of 6. These confirmations were preliminarily optimized at the PM6-D3 level by MOPAC software, from which 10 conformations with the lowest energy were selected. Subsequently, vibrational analysis was conducted employing the B3LYP-D3(BJ)/6-31 + G(d,p) method, and the conformation exhibiting the lowest free energy was depicted using the independent gradient model based on Hirshfeld partition (IGMH).[26] To qualify the intermolecular interaction energy, the sobEDAw method[27] was applied, breaking down the total interaction energy (ΔE_{int}) into four constituent terms: electrostatics (ΔE_{els}), exchange-repulsion (ΔE_{xrep}), orbital interaction (ΔE_{orb}), and dispersion (ΔE_{disp}). These terms were calculated using an ORCA with a functional and basis set of B3LYP-D3(BJ)/6-311 + G(2d,p).

$$\Delta E_{int} = \Delta E_{els} + \Delta E_{xrep} + \Delta E_{orb} + \Delta E_{disp} \quad (2)$$

The molecular conformation of individual drugs was optimized at the B3LYP-D3(BJ)/def2-TZVP level, followed by single-point energy calculations using ORCA 5.0.3 software.[28] RESP2 charge fitting[29] was performed with Multiwfn,[24] and the general AMBER force field (GAFF) parameters were generated via Sobtop software.[30] An OPC3 water model box containing 25 molecules each of PAL and GL, neutralized with Cl-, was subjected to energy optimization using the conjugate gradient minimization method. The system was preequilibrated in the NPT ensemble for 200 ps (ps) before MD simulations at 298.15 K and 1 atm, employing the v-rescale temperature and Parrinello−Rahman pressure coupling methods. The particle mesh Ewald (PME) method was adopted for electrostatic interactions with a cutoff distance of 1 nm. Production simulations were run for 50 ns, with a trajectory length of 5 ps.

Antibacterial Activity. The antibacterial activity of pure drugs and PVA-stabilized hybrid NPs/MPs was evaluated using the disk diffusion method against a panel of bacterial strains.[31] Sterile paper disks (6 mm in diameter) were impregnated with a fixed amount of an NPs/MPs suspension or drug solutions, ensuring a consistent drug concentration across all tests. The drug-loaded disks were then placed on the surfaces of freshly prepared LB plates inoculated with bacterial strains. The plates were incubated at 37 °C for 14 h. The

https://doi.org/10.1021/acsomega.4c06925
ACS Omega 2024, 9, 41990−42001

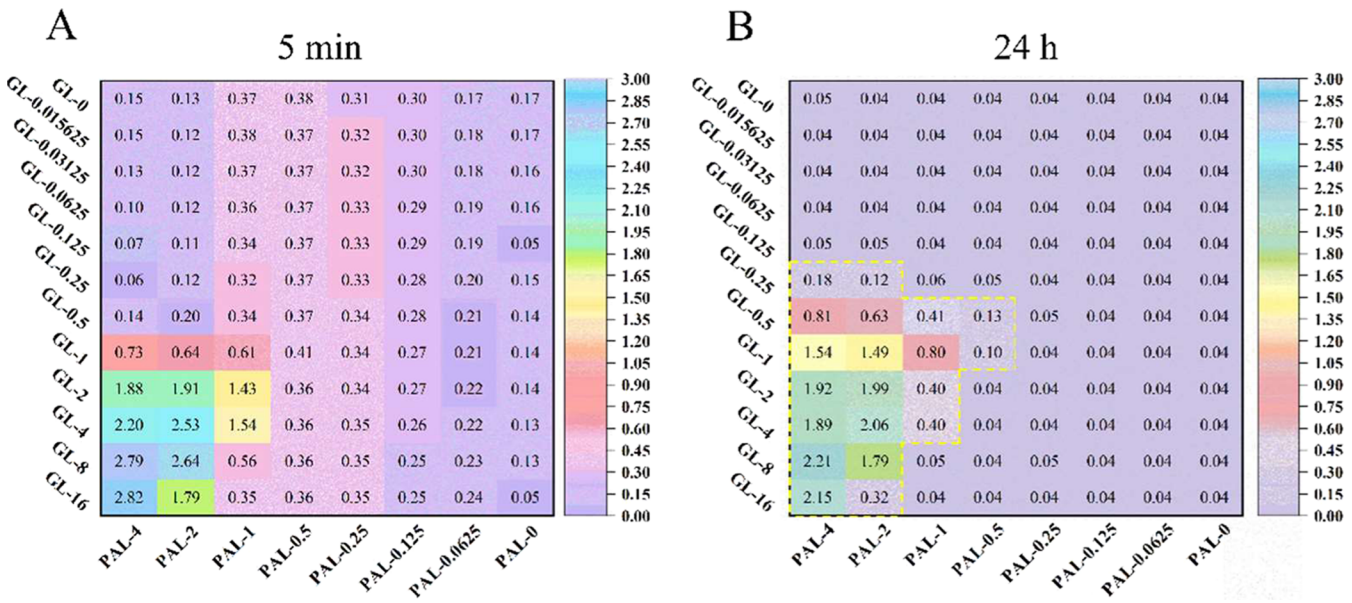

Figure 2. Heatmaps for optical density values of various aqueous solutions at different PAL and GL levels (A) before and (B) after mixing for 24 h.

formation of inhibition zones, characterized by clear areas devoid of bacterial growth around the disks, was measured in millimeters to assess the antibacterial efficacy. A positive control was established using ciprofloxacin hydrochloride as a reference antibiotic.

The minimum inhibitory concentration (MIC) of tested samples against selected bacterial strains was determined using a microdilution assay in 96-well plates.[32,33] The pure drugs or NPs/MPs were initially dissolved or dispersed in sterile water to create a stock solution. Bacterial strains were cultured in LB medium overnight, and the turbidity was adjusted to a 0.5 McFarland standard. The bacterial suspension was then diluted to a concentration of 1.0 × 106 colony-forming units (CFU)/mL. Each well of the 96-well plate was added with 100 μL of LB broth, 100 μL of bacterial suspension, and 100 μL of drug solutions at varying concentrations. The plates were incubated at 37 °C for 24 h in a controlled environment. Then, TTC solution was added to each well to serve as an indicator of bacterial growth at a final concentration of 0.5 mg/mL.[34] The plates were incubated for an additional 2 h, allowing TTC to react with metabolically active bacteria, which results in a red coloration. The MIC was identified as the lowest concentration at which no visible red color was observed, indicating the absence of bacterial growth. The mean concentration from triplicate experiments was reported as the final MIC value.

Tissue Distribution Analysis after Intravenous Administration in Rats. Male Sprague−Dawley rats (certificate number SCXK, Jing 2019-0010), weighing 210 ± 10 g, were supplied by SPF Biotechnology Co., Ltd. The study was conducted in accordance with the approval of the Ethics Committee (No. R-062022LH046) according to the "Guidelines for the Care and Use of Laboratory Animals" from the Yunnan University of Chinese Medicine.

MPs coloaded with Rhodamine B were suspended in saline and administrated via tail-vein injection. Rats were euthanized at predetermined time points postinjection to harvest heart, liver, spleen, lung, and kidney tissues. The tissues were rinsed with saline, gently blotted dry, and then imaged by an IVIS Lumina III *in vivo* imaging system (PerkinElmer). A solution of Rodamine B served as the control group.

$$\mathrm{Re} = \mathrm{FU}_{\mathrm{test}}/\mathrm{FU}_{\mathrm{control}} \quad (3)$$

$$\mathrm{Te} = \mathrm{FU}_{\mathrm{target}}/\mathrm{FU}_{\mathrm{non\text{-}target}} \quad (4)$$

The fluorescence unit (FU) values of tissues were collected to calculate the relative uptake rate (Re) and targeting efficiency (Te) of each organ using eqs 3 and 4[35]

Statistical Analysis. Data are presented as the mean ± the standard deviation (SD). Statistical analysis was performed with DAS 3.0 software. One-way analysis of variance (ANOVA) was employed for multiple group comparisons, and *t* tests were used to evaluate significant differences between two groups. A *p* value of less than 0.05 was considered statistically significant.

RESULTS AND DISCUSSION

Preparation of Hybrid Microparticles. *Drug Concentration Range for Particle Formation.* The drug concentration range for particle formation was determined by assessing the OD values of various aqueous systems. As shown in Figure 2, systems with an OD value exceeding 0.10 after 24 h were marked with a yellow dashed line, indicating a transition from a clear to a suspension or precipitate phase.

Most mixtures exhibited a decrease in OD value post storage, with visible precipitates forming in those with higher initial OD values. The high OD values observed during the initial mixing at an elevated temperature of 80 °C can be attributed to vigorous Brownian motion. After 24 h at room temperature, the systems reached an equilibrium, with the OD values accurately reflecting the turbidity. Only mixtures with OD values above 0.10 formed particulate or gel-like masses, suggesting precipitation thresholds of >0.5 mM for PAL and >0.25 mM for GL.

Optimization of Drug Ratio. To further optimize the molar ratio of PAL to GL, a series of mixtures were prepared, and their micromorphological images were depicted in Figure S1 (see Supporting File). The results indicated that the drug concentration and ratio significantly influenced particle formation. Mixtures with a high GL ratio gel-like mass (1:4 and 1:8) formed or showed a tendency to gel (1:2), likely due

https://doi.org/10.1021/acsomega.4c06925
ACS Omega 2024, 9, 41990−42001

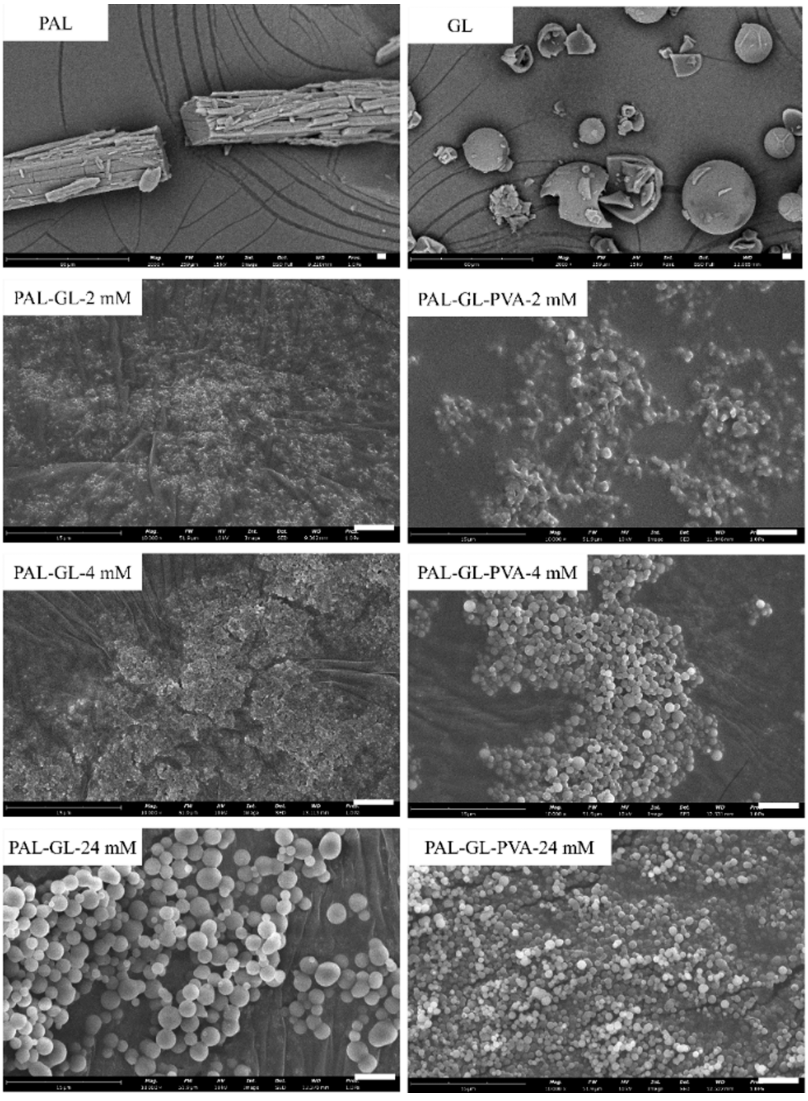

Figure 3. SEM images of pure drugs (bar size = 5 μm) and hybrid microparticles with or without PVA at different levels (bar size = 5 μm).

to GL's self-aggregating property.[36] In contrast, mixtures with a high PAL ratio showed no particle formation (16:1 and 8:1) or very few particles (4:1). A molar ratio of 2:1 for PAL and GL was identified as optimal, yielding numerous uniform and fine particles across a wide concentration range of 0.5−4 mM PAL.

Influence of PVA Addition on Pure and Mixed Systems. Figure S2 displays images of various solutions or suspensions at different drug concentrations, with and without PVA (see Supporting File). As depicted in Figure S2, the mixtures containing PAL and PVA did not show any precipitates, while pure PAL or GL solutions became turbid upon mixing. Sediment was evident in mixtures lacking PVA, whereas those with PVA maintained a uniform yellowish appearance. Under laser light, pure GL or PVA solutions showed a continuous and straight light path, characteristic of a colloidal system. In contrast, all other mixtures exhibited a diffused light path, indicating the presence of larger particles. These observations suggest that the interaction between PAL and GL can lead to the formation of particulate products in aqueous media and the addition of PVA can mitigate particle sedimentation.

These findings collectively demonstrate the pivotal role of drug concentration, ratio, and PVA in the formation and stabilization of hybrid microparticles, paving the way for their potential application in drug delivery systems.

Particle Micromorphological Observation. To delve deeper into how drug concentration and the addition of PVA influence particle morphology, the samples were examined under an optical microscope (see Figure S3 in Supporting File) and SEM (see Figure 3).

Figure 3 reveals that the yellow powders of pure PAL appeared as elongated bars exceeding 80 μm in diameter with a cracked surface under SEM. The original GL powders presented as hollow spheres, measuring 15−40 μm in size, a characteristic potentially linked to the production process of raw materials. For instance, spray drying typically yields spherical powders with porous or hollow structure.[37] The precipitates from the aqueous mixtures of PAL and GL were spherical with smooth surfaces, indicating a narrow size distribution. Notably, particle size escalated with increasing drug concentration, from less than 1 μm at 2 and 4 mM to 2−5 μm at 24 mM.

PVA, recognized for its biodegradable semicrystalline nature, serves multiple roles in pharmaceuticals, including as a solid dispersion carrier to boost drug solubility, an emulsifier for emulsion droplet and microsphere formation, and a stabilizer

https://doi.org/10.1021/acsomega.4c06925
ACS Omega 2024, 9, 41990−42001

Table 1. Analysis Results of Particle Size Distribution and ζ-Potential

formulations	mean particle size (nm)	PDI	ζ-potential (mV)
PAL-GL-2 mM	275.36 ± 2.66	0.20 ± 0.03	−16.41 ± 0.97
PAL-GL-4 mM	1360.07 ± 41.56	0.15 ± 0.03	−8.80 ± 0.60
PAL-GL-24 mM	1808.99 ± 150.79	0.52 ± 0.32	−4.97 ± 1.70
PAL-GL-PVA-2 mM	349.45 ± 7.92	0.17 ± 0.07	−7.12 ± 0.64
PAL-GL-PVA-4 mM	1978.70 ± 113.50	0.48 ± 0.17	−2.89 ± 2.67
PAL-GL-PVA-24 mM	1040.08 ± 40.63	0.55 ± 0.08	−4.79 ± 2.33

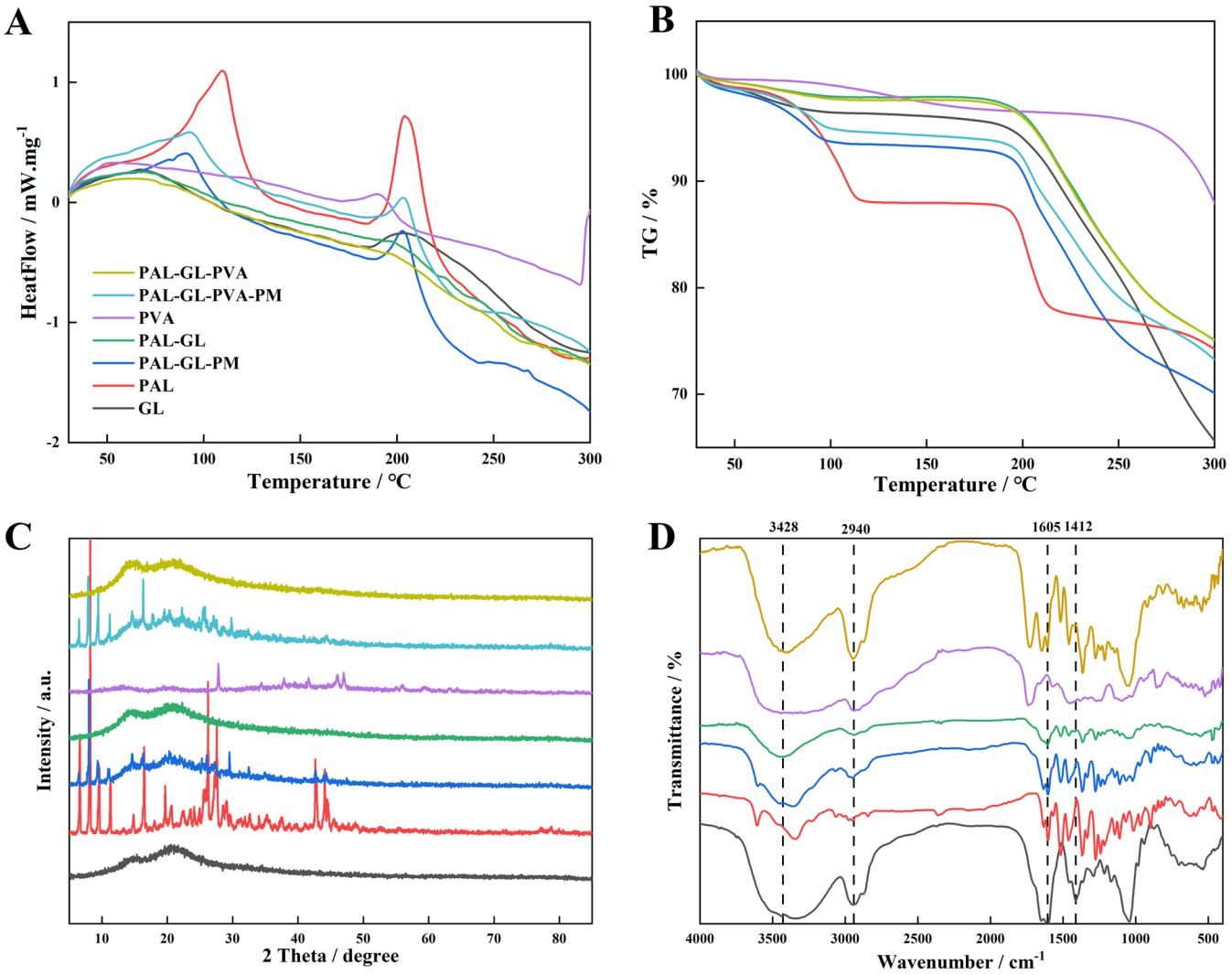

Figure 4. (A) DSC curves, (B) TG diagrams, (C) PXRD patterns, and (D) infrared spectra of pure drugs, their physical mixture, and hybrid microparticles with or without PVA.

to prevent crystal nucleation and growth.[38−40] In this study, the addition of 4 mg/mL PVA was observed to induce the larger particle formation in 2 or 4 mM mixtures but resulted in significantly smaller particles in a 24 mM mixture, all displaying a more uniform morphology and size. This suggests that PVA not only stabilizes the particles but also regulates the aggregation and growth processes, culminating in the production of more uniform and finer particles.

These observations underscore the pivotal role of PVA in tailoring particle size and uniformity, which could be instrumental in enhancing the performance of drug delivery systems.

Particle Size Distribution and ζ-Potential Analysis. The average size, polydispersity index (PDI), and ζ-potential values of various samples are listed in Table S1 (see Supporting File) and Table 1.

In the PAL solution, no particles were detected and it exhibited a nearly neutral charge, affirming its true solution state. GL solution showed a mean particle size of less than 110 nm with a negative charge of around −30 mV, attributed to its dissociation in aqueous medium.[41] PVA solution had a mean size of less than 30 nm, and the presence of PAL had a minimal effect on its size and charge.

When the drug solutions were combined, large particles were observed, with their size increasing with drug

https://doi.org/10.1021/acsomega.4c06925
ACS Omega 2024, 9, 41990−42001

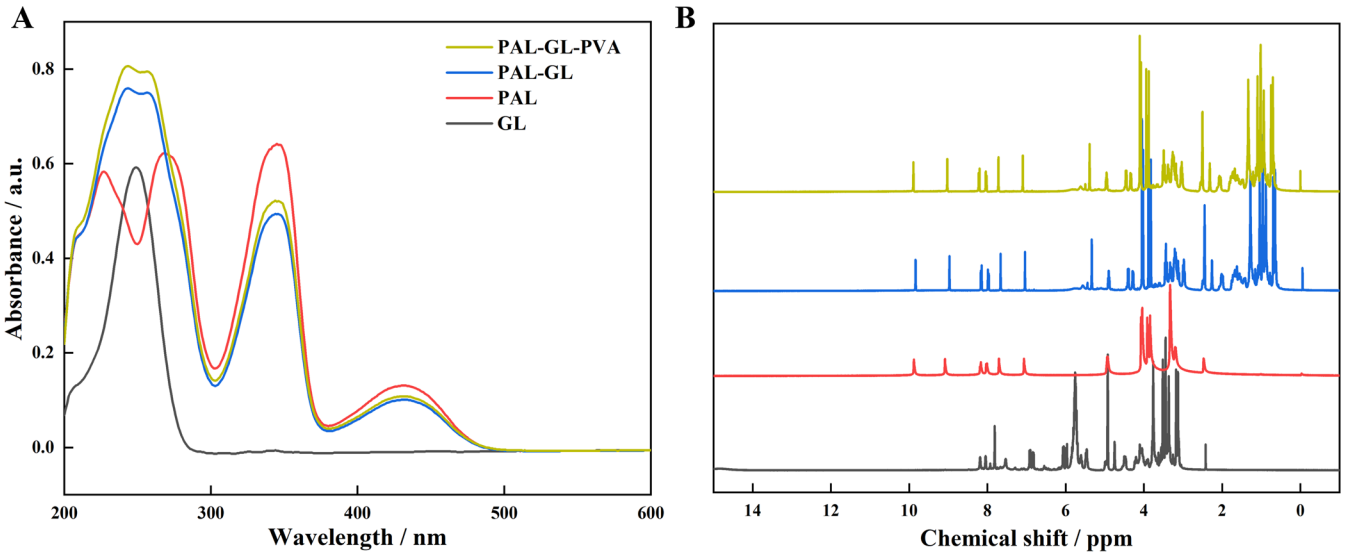

Figure 5. (A) UV−vis and (B) ^{1}H NMR spectra of pure drugs and hybrid microparticles with or without PVA.

concentration. The addition of PVA helped to standardize the size among the mixtures, showcasing its stabilizing and homogenizing effect. The formation of hybrid particles has a ζ-potential around −5.0 mV, suggesting a shielding effect of the negative charge on the particle surface. The presence of PVA had a negligible influence on the surface charge of the hybrid particles.

It should be noted that the measured sizes for samples without PVA might be lower than actual due to the potential sedimentation of larger particles during DLS analysis, particularly for the 24 mM mixture. DLS measurements reflect the hydrated size of particles in the aqueous medium, which is typically slightly larger than the sizes observed in SEM for dried particles.[42] The particles obtained at 24 mM were selected for further analysis.

Solid Characterization. *Thermal Analysis.* The thermograms depicted in Figure 4A,4B for all samples exhibited a broad endothermic effect within the temperature range of 70−100 °C, which is likely due to the release of water molecules. Two distinct endothermic peaks were observed for PAL at 109.8 and 203.8 °C,[43] while GL and PVA showed a single peak at 203.9[44,45] and 189.9 °C,[46,47] respectively. These peaks are attributed to melting or degradation events during the heating process. The physical mixtures of the two drugs, irrespective of PVA presence, maintained clear peaks around 92 and 203 °C. In contrast, the dual-drug particles exhibited no significant endothermic peaks, indicating a change in thermal behavior upon coassembly. The presence of PVA had a minimal impact on the thermal properties of the particles sample.

PXRD. The crystallinity of the powder samples was evaluated using diffractograms, as shown in Figure 4C. PAL demonstrated a crystalline structure with intense diffraction peaks between 5 and 50°, in line with previous reports.[43,24] PVA powder displayed several peaks within the 2θ range of 25−50°.[45] Conversely, GL appeared amorphous, lacking high-intensity peaks, potentially due to the self-aggregation of the drug molecules.[46] The physical mixture exhibited multiple diffraction peaks at 2θ of 6, 8, 9, 26, and 27° with reduced intensity, attributable to PAL. The PAL-GL hybrid particles revealed only two broad peaks within the 2θ range of 10−30°, suggesting an amorphous state of the complexed particles during the coassembly process in aqueous media. The crystalline state of the samples was not significantly affected by the presence of PVA, indicating its minimal influence on the crystallinity.

FTIR. Potential interactions among PAL, GL, and PVA were analyzed using FTIR spectroscopy, as presented in Figure 4D. GL exhibited characteristic bands at 3345 cm^{-1} (hydroxyl in the carboxyl group), 2947 cm^{-1} (methyl), 1649 cm^{-1} (carbonyl), and 1412 cm^{-1} (carboxyl in glucuronic acid). For PAL, bands at 2946, 1633, and 1568 cm^{-1} were assigned to the stretching vibrations of the methoxy group and C−N bond. Notable shifts in the PAL-GL spectrum were observed a blue shift from 3345 to 3428 cm^{-1}, red shifts from 2947 to 2941 cm^{-1} and from 1649 to 1605 cm^{-1}; the original absorptions at 1412 and 1568 cm^{-1} were no longer present. A similar spectrum was observed for the PAL-GL complex with PVA, albeit with increased peak intensities. These spectral changes suggest possible steric interactions and hydrogen bond formation between PAL and GL molecules.

Liquid Characterization. *UV−Vis Spectroscopy.* The UV−vis spectra of the original drugs and hybrid particles were examined, as shown in Figure 5A. PAL displayed four principle absorption peaks at peak values of 227, 268, 345, and 432 nm, corresponding to the characteristic absorptions of homocyclodiene, benzene ring, quaternary ammonium, and conjugated double bonds, respectively. Pure GL exhibited a maximum absorption band at 249 nm, which is attributed to its carboxyl group.[44] In the spectrum of PAL-GL hybrid particles, the principle absorption bands of PAL and GL merged into a broad peak around 250 nm with increased intensity, while the peaks at 346 and 432 nm for PAL showed reduced intensity. Notably, PVA, which is nonabsorptive in the UV range, did not significantly affect the spectra of particles. These observations suggest the presence of intermolecular interactions between the quaternary ammonium group of PAL and the carboxyl group of GL, with PVA exerting a minimal influence on the spectral characteristics of the PAL-GL complex.

^{1}H NMR Spectrometry. To further clarify the nature and position of molecular interactions between PAL and GL, the ^{1}H NMR spectra of the hybrid particles were obtained and compared to those of the individual compounds. The chemical

https://doi.org/10.1021/acsomega.4c06925
ACS Omega 2024, 9, 41990−42001

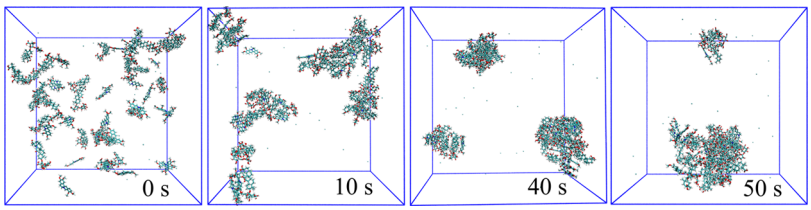

Figure 6. Snapshots for the complexation of PAL and GL during the molecular dynamic simulation process.

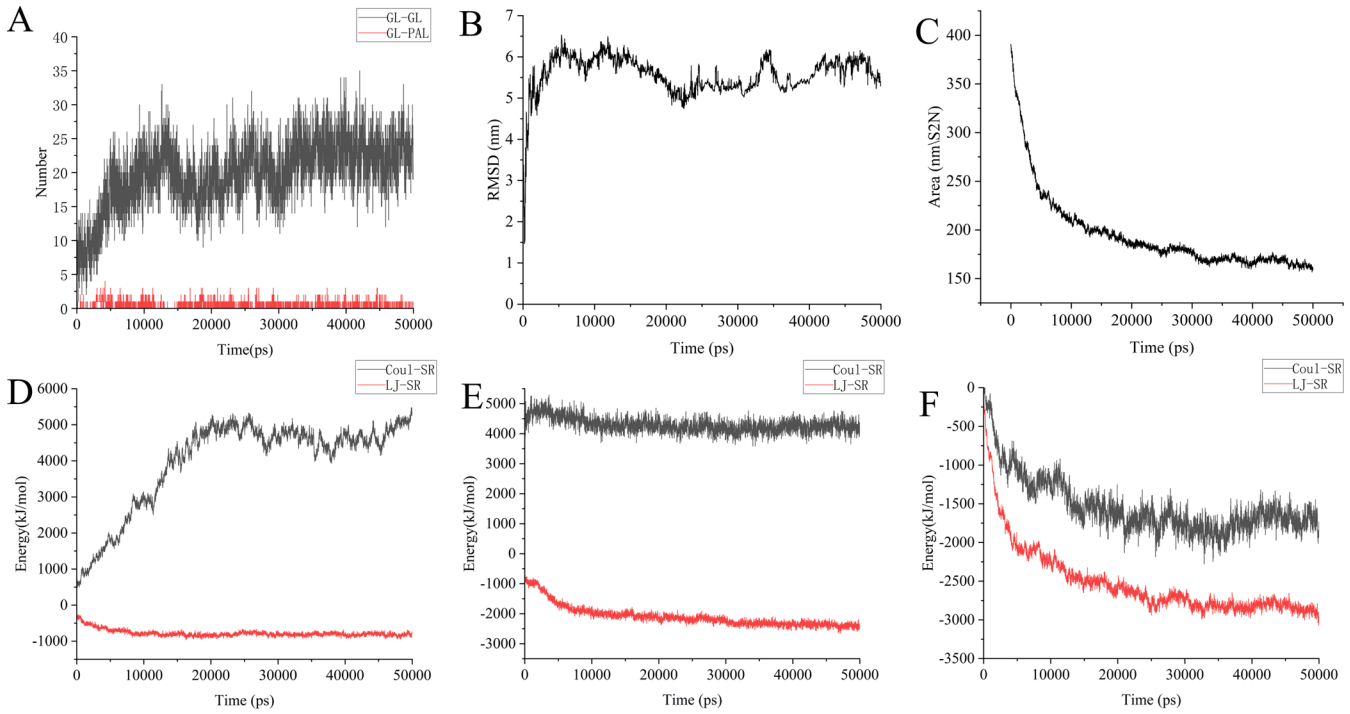

Figure 7. (A) Number of drug−drug hydrogen bonds, (B) solvent-accessible surface area, (C) RMSD value of the PAL-GL complex, and energy change of (D) PAL−PAL, (E) GL-GL, and (F) PAL-GL systems during the MD simulation process.

shifts and assignments of the hydrogen signals are detailed in Tables S2 and S3 (see Supporting File). Following the coassembly of PAL and GL, the H signals for PAL shifted upfield from 9.87, 9.08, and 4.94 ppm to 9.83, 8.97, and 4.90 ppm, respectively. Concurrently, the OCH_3 signals shifted downfield from 3.91 and 3.83 to 4.01 and 3.88 ppm, respectively. PVA-stabilized particles displayed a similar spectrum pattern. The H signals associated with glucuronic acid and the OCH_3 signals of GL also underwent a slight shift. These findings indicate that PAL and GL molecules are involved in $\pi-\pi$ stacking and steric interactions, which are key to the stability and properties of the hybrid particles.

Drug Content. The drug content within the dried PVA-stabilized particles was measured at 20.54 ± 0.19% for PAL and 52.06 ± 0.52% for GL, respectively. This translates to a total drug loading of over 70% for the particles, marking a notable enhancement in comparison to those prepared by conventional methods and polymer carriers.

The molar ratio of PAL to GL in the hybrid particles was approximately 0.8:1, nearing the 1:1 ratio and aligning with the MD analysis outcomes. Interestingly, despite the initial aqueous mixture's 2:1 ratio, the final particle product showed a significant increase in PAL content. This increase is attributed to the equilibrium established during the spontaneous coassembly process. The remaining drug molecules, still present in the solution, could be harnessed in further reaction cycles. The complexation mechanism of PAL with GL at a 1:1 molar ratio was further dissected to elucidate the underlying interactions.[48]

Molecular Dynamic Simulations. To gain a comprehensive understanding of the interaction between PAL and GL during coassembly, MD simulations were conducted, focusing on intermolecular interactions, energetics, and aggregation process.

Figure S4A presents a detailed map of the intermolecular interactions, with the IGMH maps highlighting van der Waals interactions and hydrogen bonding between PAL and GL molecules. The GL-GL complex displayed relatively stronger hydrogen bonding and van der Waals interactions, suggesting a propensity for self-association.

Table S4 details the interaction energies for the GL-GL and PAL-GL dimers. Both dimers exhibited negative electrostatic terms, indicative of attractive forces. The positive exchange-repulsion term points to repulsive interactions that may be counteracted by other attractive forces. The orbital interaction term, representing the energy associated with the overlap of molecular orbitals, varies between the two dimers. The dispersion term, a measure of van der Waals interactions, significantly contributed to the total interaction energy for both dimers, emphasizing the role of noncovalent interactions

https://doi.org/10.1021/acsomega.4c06925
ACS Omega 2024, 9, 41990−42001

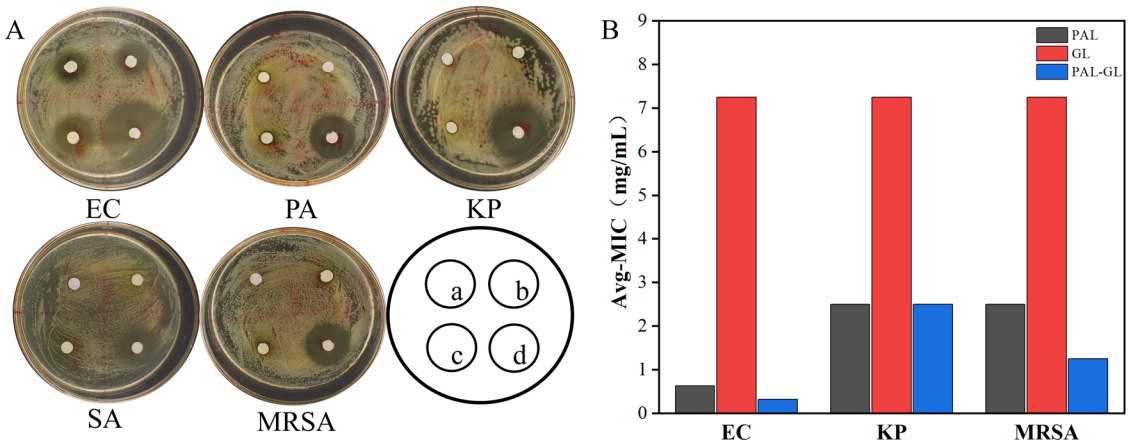

Figure 8. (A) Inhibition zone and (B) MIC values for (a) pure PAL or (b) GL, (c) hybrid MPs, and (d) ciprofloxacin against various bacterial strains.

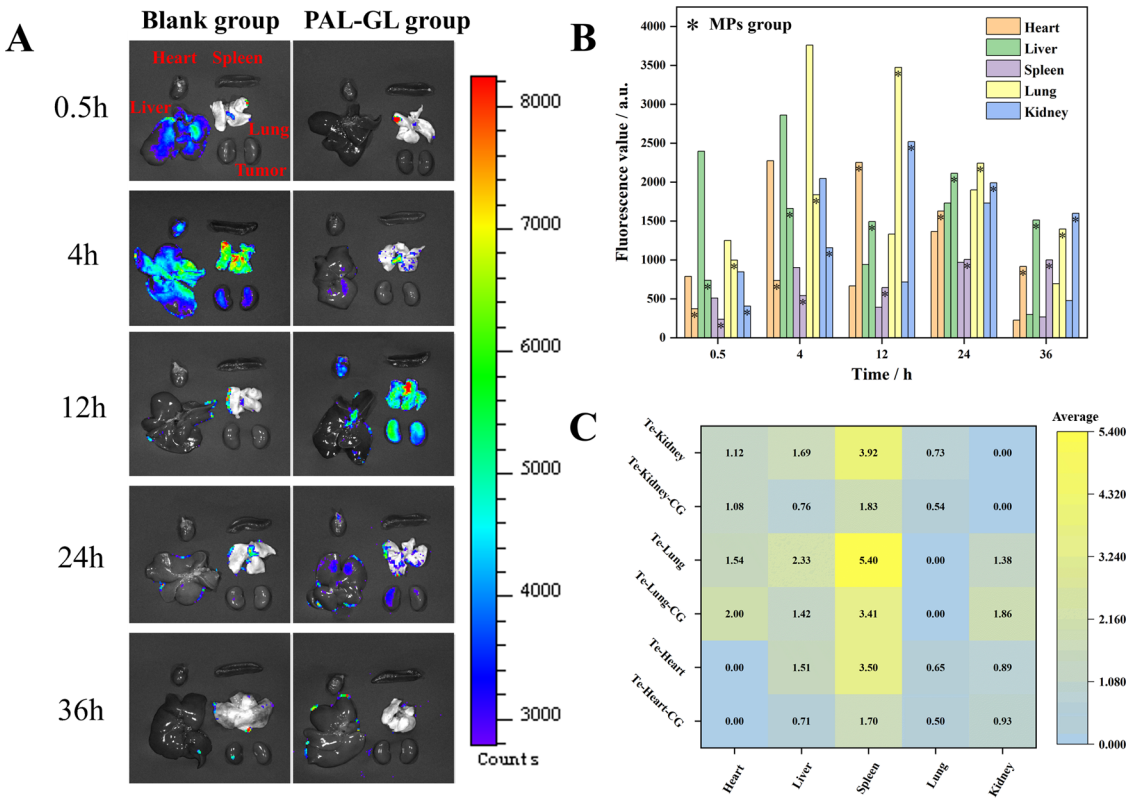

Figure 9. (A) Images, (B) fluorescence units of various rat tissues at different time points, and (C) targeting parameters for the control and PVA-stabilized MPs group.

in complex stabilization. The negative total interaction energy values suggest spontaneous complex formation between GL and PAL or GL, with the GL-GL complex showing a potentially stronger binding affinity due to its lower ΔE_{int} value. The differences in interaction energies may be attributed to the distinct molecular structures and electronic configurations of PAL and GL.

Figure 6 illustrates snapshots of the complexation process between PAL and GL. Initially, 50 molecules of each were dispersed in the water box. Aggregates formed within 10 ns due to hydrophobic interactions and further assembled into larger structures by 40 ns, driven by $\pi-\pi$ stacking within the polycyclic backbones of the drug molecules.

Key parameters from the MD simulation are depicted in Figure 7. The number of hydrogen bonds between GL molecules peaked at 25 within the first 10 ns, with no significant hydrogen bonding observed between the PAL-GL molecules. The RMSD value of the system reached approximately 6.0 nm in the first 5 ns and then fluctuated around this level. The solvent-accessible surface area decreased significantly from 390 to 160 nm^2 within 50 ns and reached an equilibrium state, indicating a transition to a more compact state.

The electrostatic interaction (represented by Coul-SR) and van der Waals interaction (represented by LJ-SR) were analyzed. The positive system energy values (Figure 7D,E) indicated strong electrostatic repulsion between PAL−PAL

https://doi.org/10.1021/acsomega.4c06925
ACS Omega 2024, 9, 41990−42001

and GL-GL molecules, with the former increasing and the latter slightly decreasing during the simulation. Conversely, the van der Waals interaction showed a slight decline for the two drug dimers. However, both electrostatic attraction and van der Waals interactions between PAL-GL molecules intensified throughout the simulation (Figure 7F).

The intermolecular interaction analysis, complemented by the MD simulations, confirmed that the complexation between PAL and GL is primarily facilitated by intermolecular hydrogen bonding and $\pi-\pi$ stacking. These interactions are crucial for the formation of stable precipitates in the aqueous solution system, as observed in the simulations. The solvent effect plays a pivotal role in mediating the electrostatic repulsion between the positively charged PAL molecules, allowing for the formation of dimer within the water box.

Antibacterial Activity. The antibacterial efficacy of PVA-stabilized particles was evaluated against various bacterial strains with results compared with those of the pure drugs. The disk diffusion and MIC results are presented in Figure 8.

In accordance with the Clinical and Laboratory Standards Institute (CLSI) guidelines, the pure PAL or GL showed moderate sensitivity against EC with inhibition zone diameters between 10 and 15 mm. They exhibited low sensitivity (7−9 mm) or were nonsensitive to the other strains tested. The particles, however, demonstrated a larger inhibition zone against EC, PA, and MRSA, suggesting a potent antibacterial effect. Moreover, the MIC values for the particles were significantly lower than those of pure PAL for EC and MRSA, indicating a potential for enhanced therapeutic efficacy in the particle form.

These findings suggest that the particle formulation may provide a superior delivery method for PAL and GL, especially against specific bacterial strains. This could be due to the synergistic interactions within the hybrid particle system or the modified pharmacokinetics of the encapsulated drugs.[49,50] The superior antibacterial activity of the particles compared with the pure drugs highlights their potential as a promising strategy for developing innovative antimicrobial agents.

Tissue Distribution Analysis. The biodistribution performance of Rodamine B after intravenous injection of PVA-stabilized particles was accessed with the corresponding solution serving as a control. The main tissues of both groups were imaged at various time points (Figure 9A), after which FU values (Figure 9B) and targeting parameters (Figure 9C) were compared.

In the control group, intense fluorescence was observed in the liver 0.5 h postadministration, with fluorescence spreading to all organs except the spleen by 4 h, and a notable decrease in fluorescence intensity after 12 h. In contrast, the particle group showed high FU in the lung and liver at 0.5 and 4 h, with peak FU values in the heart, lung, and kidney at 12 h, after which a gradual decline was observed. The targeting parameters revealed that the particles group had a significant targeting capacity and increased selectivity for the kidney, lung, and heart tissues compared to the control group.[51] The enhanced tissue distribution of the particles suggests potential benefits for the treatment of diseases associated with specific organs.[52]

CONCLUSIONS

This study successfully developed PVA-stabilized NPs/MPs designed for the codelivery of PAL and GL. The supramolecular interactions between PAL and GL, including $\pi-\pi$ stacking and hydrogen bonding, facilitated the formation of hybrid particles through a coassembly process. These particles demonstrated a high drug loading of over 70% as uniform microspheres with a nearly neutral charge. Both in vitro antibacterial activity and in vivo biodistribution of the resulting NPs/MPs were found to be superior to that of the control group, indicated enhanced bioactive and targeting performance, and highlighted a potential for treating organ-specific diseases.

In summary, the PVA-stabilized hybrid NPs/MPs constitute a promising platform for the codelivery of natural products, offering advantages in terms of drug loading, stability, and targeted delivery. These findings lay the groundwork for the further development and clinical application of this novel drug delivery system. Future studies will focus on exploring the synergistic antibacterial effects of these high-payload PVA-stabilized NPs/MPs, as well as evaluating their in vivo biocompatibility and therapeutic efficacy for combating bacterial infections.

ASSOCIATED CONTENT

Supporting Information

The Supporting Information is available free of charge at https://pubs.acs.org/doi/10.1021/acsomega.4c06925.

Images of PAL-GL mixtures (Figure S1); appearance and Tyndall effect of PAL-GL mixtures (Figure S2); micrographs of PAL-GL mixtures with and without PVA (Figure S3); particle size and ζ-potential data (Table S1); ^{1}H NMR chemical Shifts of PAL (Table S2) and GL (Table S3); IGMH maps (Figure S4); and interaction energy (Table S4) of PAL-GL complex (PDF)

AUTHOR INFORMATION

Corresponding Authors

Peng Zhang − *General Hospital of Ningxia Medical University, Yinchuan, Ningxia 750004, China*; Phone: +86-9516743353; Email: zhp435656@163.com

Wenping Wang − *College of Chinese Materia Medica, Yunnan University of Chinese Medicine, Kunming, Yunnan 650500, China*; orcid.org/0009-0009-6115-3880; Phone: +-86-87167495503; Email: Email: wangwenping@ynucm.edu.cn

Authors

Hua Yang − *College of Chinese Materia Medica, Yunnan University of Chinese Medicine, Kunming, Yunnan 650500, China*

Yuerui Yang − *College of Chinese Materia Medica, Yunnan University of Chinese Medicine, Kunming, Yunnan 650500, China*

Jiao Wang − *College of Chinese Materia Medica, Yunnan University of Chinese Medicine, Kunming, Yunnan 650500, China*

Zhi Dong − *College of Chinese Materia Medica, Yunnan University of Chinese Medicine, Kunming, Yunnan 650500, China*

Jiali Wang − *College of Chinese Materia Medica, Yunnan University of Chinese Medicine, Kunming, Yunnan 650500, China*

Yuhua Ma − *Key Laboratory for Tibet Plateau Phytochemistry of Qinghai Province, School of Pharmacy, Qinghai Nationalities University, Xining, Qinghai 810007, China*

https://doi.org/10.1021/acsomega.4c06925
ACS Omega 2024, 9, 41990−42001

Complete contact information is available at:
https://pubs.acs.org/10.1021/acsomega.4c06925

Author Contributions

‖H.Y. and Y.Y. contributed equally to this work as the co-first authors.

Notes

The authors declare no competing financial interest.

■ ACKNOWLEDGMENTS

This work was supported by the Applied Basic Research Joint Special Funds on Chinese Medicine of Yunnan Provincial Science and Technology Department (202301AZ070001-059, 202001AZ070001-011) for their financial support. This work was also partly supported by Natural Science Foundation of Ningxia Hui Autonomous Region (2022AAC03578) and the Open Project Program of Yunnan Key Laboratory of Southern Medicinal Utilization (202105AG070012XS23064, 202105AG070012XS23065). The authors are grateful to the Reserved Talents Project for Young and Middle-Aged Academic and Technical Leaders of Yunnan Province (202205AC160038).

■ REFERENCES

(1) Dubey, S. K.; Parab, S.; Achalla, V. P. K.; Narwaria, A.; Sharma, S.; Jaswanth Gowda, B. H.; Kesharwani, P. Microparticulate and nanotechnology mediated drug delivery system for the delivery of herbal extracts. *J. Biomater. Sci., Polym. Ed.* **2022**, *33* (12), 1531−1554.

(2) (a) Huo, Y.; Singh, P.; Kim, Y. J.; et al. Biological synthesis of gold and silver chloride nanoparticles by Glycyrrhiza uralensis and in vitro applications. *Artif. Cells, Nanomed., Biotechnol.* **2018**, *46* (2), 303−312. (b) Birk, S. E.; Boisen, A.; Nielsen, L. H. Polymeric nano- and microparticulate drug delivery systems for treatment of biofilms. *Adv. Drug Delivery Rev.* **2021**, *174* (Jul), 30−52.

(3) Moore, T. L.; Cook, A. B.; Bellotti, E.; et al. Shape-specific microfabricated particles for biomedical applications: a review. *Drug Delivery Transl. Res.* **2022**, *12*, 2019−2037.

(4) da Silva, R. Y. P.; de Menezes, D. L. B.; Oliveira, V. D. S.; Converti, A.; de Lima, ÁAN. Microparticles in the Development and Improvement of Pharmaceutical Formulations: An Analysis of In Vitro and In Vivo Studies. *Int. J. Mol. Sci.* **2023**, *24* (6), 5441.

(5) Lukova, P.; Katsarov, P.; Pilicheva, B. Application of Starch, Cellulose, and Their Derivatives in the Development of Microparticle Drug-Delivery Systems. *Polymers* **2023**, *15* (17), 3615.

(6) Wang, H.; Zhang, G.; Ma, X.; Liu, Y.; Feng, J.; Park, K.; Wang, W. Enhanced encapsulation and bioavailability of breviscapine in PLGA microparticles by nanocrystal and water-soluble polymer template techniques. *Eur. J. Pharm. Biopharm.* **2017**, *115* (Jun), 177−185.

(7) Procopio, A.; Lagreca, E.; Jamaledin, R.; La Manna, S.; Corrado, B.; Di Natale, C.; Onesto, V. Recent Fabrication Methods to Produce Polymer-Based Drug Delivery Matrices (Experimental and In Silico Approaches). *Pharmaceutics* **2022**, *14* (4), 872.

(8) Etter, E. L.; Mei, K. C.; Nguyen, J. Delivering more for less: nanosized, minimal-carrier and pharmacoactive drug delivery systems. *Adv. Drug Delivery Rev.* **2021**, *179* (Dec), No. 113994.

(9) Yu, L.; Jin, Y.; Song, M.; Zhao, Y.; Zhang, H. When Natural Compounds Meet Nanotechnology: Nature-Inspired Nanomedicines for Cancer Immunotherapy. *Pharmaceutics* **2022**, *14* (8), 1589.

(10) Fu, S.; Li, G.; Zang, W.; Zhou, X.; Shi, K.; Zhai, Y. Pure drug nano-assemblies: A facile carrier-free nanoplatform for efficient cancer therapy. *Acta Pharm. Sin B* **2022**, *12* (1), 92−106.

(11) Zeng, L.; Gowda, B. H. J.; Ahmed, M. G.; et al. Advancements in nanoparticle-based treatment approaches for skin cancer therapy. *Mol. Cancer* **2023**, *22*, 10.

(12) Li, G.; Sun, B.; Li, Y.; Luo, C.; He, Z.; Sun, J. Small-Molecule Prodrug Nanoassemblies: An Emerging Nanoplatform for Anticancer Drug Delivery. *Small* **2021**, *17* (52), No. e2101460.

(13) Li, F.; Zhe, T.; Ma, K.; Li, R.; Li, M.; Liu, Y.; Cao, Y.; Wang, L. A Naturally Derived Nanocomposite Film with Photodynamic Antibacterial Activity: New Prospect for Sustainable Food Packaging. *ACS Appl. Mater. Interfaces* **2021**, *13* (44), 52998−53008.

(14) Li, H.; Zang, W.; Mi, Z.; Li, J.; Wang, L.; Xie, D.; Zhao, L.; Wang, D. Tailoring carrier-free nanocombo of small-molecule prodrug for combinational cancer therapy. *J. Controlled Release* **2022**, *352* (Dec), 256−275.

(15) Long, J.; Song, J.; Zhong, L.; Liao, Y.; Liu, L.; Li, X. Palmatine: A review of its pharmacology, toxicity and pharmacokinetics. *Biochimie* **2019**, *162* (Jul), 176−184.

(16) Tarabasz, D.; Kukula-Koch, W. Palmatine: A review of pharmacological properties and pharmacokinetics. *Phytother Res.* **2020**, *34* (1), 33−50.

(17) Shinu, P.; Gupta, G. L.; Sharma, M.; Khan, S.; Goyal, M.; Nair, A. B.; Kumar, M.; Soliman, W. E.; Rahman, A.; Attimarad, M.; Venugopala, K. N.; Altaweel, A. A. A. Pharmacological Features of 18β-Glycyrrhetinic Acid: A Pentacyclic Triterpenoid of Therapeutic Potential. *Plants* **2023**, *12* (5), 1086.

(18) Shi, F.; Chen, L.; Wang, Y.; et al. Enhancement of oral bioavailability and anti-hyperuricemic activity of aloe emodin via novel Soluplus—glycyrrhizic acid mixed micelle system. *Drug Delivery Transl. Res.* **2022**, *12*, 603−614.

(19) Selyutina, O. Y.; Polyakov, N. E. Glycyrrhizic acid as a multifunctional drug carrier—From physicochemical properties to biomedical applications: A modern insight on the ancient drug. *Int. J. Pharm.* **2019**, *559* (Mar 25), 271−279.

(20) Stecanella, L. A.; Bitencourt, A. P. R.; Vaz, G. R.; Quarta, E.; Silva Júnior, J. O. C.; Rossi, A. Glycyrrhizic Acid and Its Hydrolyzed Metabolite 18β-Glycyrrhetinic Acid as Specific Ligands for Targeting Nanosystems in the Treatment of Liver Cancer. *Pharmaceutics* **2021**, *13* (11), 1792.

(21) Zheng, T.; Chen, H.; Wu, C.; Wang, J.; Cui, M.; Ye, H.; Feng, Y.; Li, Y.; Dong, Z. Fabrication of Co-Assembly from Berberine and Tannic Acid for Multidrug-Resistant Bacteria Infection Treatment. *Pharmaceutics* **2023**, *15* (7), 1782.

(22) Van Der Spoel, D.; Lindahl, E.; Hess, B.; Groenhof, G.; Mark, A. E.; Berendsen, H. J. GROMACS: fast, flexible, and free. *J. Comput. Chem.* **2005**, *26* (16), 1701−1718.

(23) Lu, T. *Molclus Program*. Version 1.9. http://www.keinsci.com/research/molclus.html.

(24) Lu, T.; Chen, F. Multiwfn: A multifunctional wavefunction analyzer. *J. Comput. Chem.* **2012**, *33*, 580−592.

(25) Humphrey, W.; Dalke, A.; Schulten, K.; et al. VMD: visual molecular dynamics. *J. Mol. Graphics* **1996**, *14* (1), 33−38.

(26) Lu, T.; Chen, Q. Independent gradient model based on Hirshfeld partition: A new method for visual study of interactions in chemical systems. *J. Comput. Chem.* **2022**, *43*, 539−555.

(27) Lu, T.; Chen, Q. Simple, Efficient, and Universal Energy Decomposition Analysis Method Based on Dispersion-Corrected Density Functional Theory. *J. Phys. Chem. A* **2023**, *127* (33), 7023−7035.

(28) Neese, F. Software update: The ORCA program system—Version 5.0. *WIREs Comput. Mol. Sci.* **2022**, *12*, No. e1606.

(29) Schauperl, M.; Nerenberg, P. S.; Jang, H.; et al. Non-bonded force field model with advanced restrained electrostatic potential charges (RESP2). *Commun. Chem.* **2020**, *3*, 44.

(30) Lu, T. *Sobtop*. Version 1.0(dev 3.1). http://sobereva.com/soft/Sobtop.

(31) Du, J.; Fu, J.; Chen, T. Investigation of the Antibacterial Properties and Mode of Action of Compounds From Urtica dioica L. *Cureus* **2024**, *16* (1), No. e52083.

(32) Atul, A.; Suresh, K.; Harsha, S.; et al. Synthesis and characterization of Drymaria cordata mediated encapsulation of Zeolitic Imidazolate Framework-8 and their antibacterial action

against drugs resistant bacteria. *Inorg. Chem. Commun.* **2023**, *157*, No. 111394.
(33) Catteau, L.; Reichmann, N. T.; Olson, J.; Pinho, M. G.; Nizet, V.; Van Bambeke, F.; Quetin-Leclercq, J. Synergy between Ursolic and Oleanolic Acids from Vitellaria paradoxa Leaf Extract and β-Lactams against Methicillin-Resistant *Staphylococcus aureus*: In Vitro and In Vivo Activity and Underlying Mechanisms. *Molecules* **2017**, *22* (12), 2245.
(34) Veiga, A.; Maria da Graça, T. T.; Rossa, L. S.; et al. Colorimetric microdilution assay: Validation of a standard method for determination of MIC, IC50%, and IC90% of antimicrobial compounds. *J. Microbiol. Methods* **2019**, *162* (Jul), 50−61.
(35) Chen, J.; Chen, Y.; Cheng, Y.; Gao, Y. Glycyrrhetinic Acid Liposomes Containing Mannose-Diester Lauric Diacid-Cholesterol Conjugate Synthesized by Lipase-Catalytic Acylation for Liver-Specific Delivery. *Molecules* **2017**, *22* (10), 1598.
(36) Tucker, I. M.; Burley, A.; Petkova, R. E.; Hosking, S. L.; Penfold, J.; Thomas, R. K.; Li, P. X.; Webster, J. R. P.; Welbourn, R.; Doutch, J. Adsorption and self-assembly properties of the plant based biosurfactant, Glycyrrhizic acid. *J. Colloid Interface Sci.* **2021**, *598* (Sep 15), 444−454.
(37) Son, Y. J.; Miller, D. P.; Weers, J. G. Optimizing Spray-Dried Porous Particles for High Dose Delivery with a Portable Dry Powder Inhaler. *Pharmaceutics* **2021**, *13* (9), 1528.
(38) Teodorescu, M.; Bercea, M.; Morariu, S. Biomaterials of PVA and PVP in medical and pharmaceutical applications: Perspectives and challenges. *Biotechnol. Adv.* **2019**, *37* (1), 109−131.
(39) Rivera-Hernández, G.; Antunes-Ricardo, M.; Martínez-Morales, P.; Sánchez, M. L. Polyvinyl alcohol based-drug delivery systems for cancer treatment. *Int. J. Pharm.* **2021**, *600* (May 1), No. 120478.
(40) Song, B.; Cho, C. W. Applying polyvinyl alcohol to the preparation of various nanoparticles. *J. Pharm. Invest.* **2024**, *54*, 249−266.
(41) Dai, X.; Liao, Y.; Yang, C.; Zhang, Y.; Feng, M.; Tian, Y.; Qu, Q.; Sheng, M.; Li, Z.; Peng, X.; Cen, S.; Shi, X. Diammonium Glycyrrhizinate-Based Micelles for Improving the Hepatoprotective Effect of Baicalin: Characterization and Biopharmaceutical Study. *Pharmaceutics* **2023**, *15* (1), 125.
(42) Wang, W.; Lei, Y.; Sui, H.; Zhang, W.; Zhu, R.; Feng, J.; Wang, H. Fabrication and evaluation of nanoparticle-assembled BSA microparticles for enhanced liver delivery of glycyrrhetinic acid. *Artif. Cells, Nanomed., Biotechnol.* **2017**, *45* (4), 740−747.
(43) Zhang, Y.; Sun, J.; Liu, L.; Chang, L.; Ji, Y.; Sun, W.; Li, J.; Feng, Y.; Geng, Y.; Cheng, G.; Gong, Y.; Guo, Y.; Wu, L.; Wang, C.; Liu, Y.; Zhang, X. Improving hygroscopic stability of palmatine by replacing $C\bar{l}$ and preparing single crystal of palmatine-salicylic acid. *J. Mol. Struct.* **2022**, *1257*, No. 132521.
(44) Kong, R.; Zhu, X.; Meteleva, E. S.; Chistyachenko, Y. S.; Suntsova, L. P.; Polyakov, N. E.; Khvostov, M. V.; Baev, D. S.; Tolstikova, T. G.; Yu, J.; Dushkin, A. V.; Su, W. Enhanced solubility and bioavailability of simvastatin by mechanochemically obtained complexes. *Int. J. Pharm.* **2017**, *534* (1−2), 108−118.
(45) Xu, W.; Wen, M.; Yu, J.; Zhang, Q.; Polyakov, N. E.; Dushkin, A. V.; Su, W. Mechanochemical preparation of kaempferol intermolecular complexes for enhancing the solubility and bioavailability. *Drug Dev. Ind. Pharm.* **2018**, *44*, 1924−1932, DOI: 10.1080/03639045.2018.1503292.
(46) Deshpande, D. S.; Bajpai, R.; Bajpai, A. K.et al. On the Development of Thermally Stable Semi-IPNs of PVA and PAN using IR, DSC and XRD Studies. In *AIP Conference Proceedings*, 2011; Vol. 1349, pp 180−181.
(47) Wlodarski, K.; Zhang, F.; Liu, T.; et al. Synergistic Effect of Polyvinyl Alcohol and Copovidone in Itraconazole Amorphous Solid Dispersions. *Pharm. Res.* **2018**, *35*, 16.
(48) Yi, L.; Xu, X. Study on the precipitation reaction between baicalin and berberine by HPLC. *J. Chromatogr. B* **2004**, *810* (1), 165−168.
(49) Huang, X.; Liu, X.; Lin, X.; Yuan, Z.; Zhang, Y.; Wang, Z.; Pi, W.; Zhao, H.; Lei, H.; Wang, P. Thermodynamics driving phytochemical self-assembly morphological change and efficacy enhancement originated from single and co-decoction of traditional chinese medicine. *J. Nanobiotechnol.* **2022**, *20* (1), 527.
(50) Li, T.; Wang, P.; Guo, W.; Huang, X.; Tian, X.; Wu, G.; Xu, B.; Li, F.; Yan, C.; Liang, X. J.; Lei, H. Natural Berberine-Based Chinese Herb Medicine Assembled Nanostructures with Modified Antibacterial Application. *ACS Nano* **2019**, *13* (6), 6770−6781.
(51) Qian, J.; Zha, L.; Wang, B.; Zhang, C.; Hong, L.; Chen, W. Synthesis, cytotoxicity and liver targeting of 3-O-β-D-Galactosylated Resveratrol. *J. Pharm. Pharmacol.* **2019**, *71* (6), 929−936.
(52) Wang, W.; Cai, Y.; Zhang, G.; Liu, Y.; Sui, H.; Park, K.; Wang, H. Sophoridine-loaded PLGA microspheres for lung targeting: preparation, in vitro, and in vivo evaluation. *Drug Delivery* **2016**, *23* (9), 3674−3680.

https://doi.org/10.1021/acsomega.4c06925
ACS Omega 2024, 9, 41990−42001